The experimental conditions for Compton scattering in the electron microscope

1993 J. Phys.: Condens. Matter 5 7173

(http://iopscience.iop.org/0953-8984/5/39/006)

J. Phys.: Condens. Matter 5 (1993) 7173–7188. Printed in the UK

The experimental conditions for Compton scattering in the electron microscope

Peter Jonas† and Peter Schattschneider†‡

† Institut für Angewandte und Technische Physik, Technische Universität Wien, Wiedner Hauptstraße 8–10, A-1040 Wien, Austria

‡ Ecole Centrale Paris, Laboratoire de Mecanique, F-92295 Chatenay-Malabry, France

Received 25 January 1993

Abstract. Electron Compton scattering from solids (ECOSS) is a technique for obtaining the momentum density distribution of charge carriers in a solid on a scale of μm or less. We discuss the possibilities and the problems of this experimental technique, which uses a conventional transmission electron microscope (CTEM) equipped with a parallel electron energy-loss spectrometer (PEELS). Favourable experimental conditions are proposed, including a scattering geometry that minimizes contributions from Bragg scattering. The procedures leading from raw spectra to Compton profiles that can be compared with theoretical predictions are described, with emphasis on background handling and deconvolution. It is shown that experiments agree well with theory. An ultimate momentum resolution of 0.05 atomic units appears feasible.

1. Introduction

Inelastic scattering of electrons or photons on target electrons at rest results in an definite increase of wavelength of the incident wave (or, equivalently, loss of energy of the probing particle). The change in wavelength is known as Compton shift (Compton 1922). For a moving scatterer, the Compton shift will be different in general, but it will still have a definite value. The energy-loss spectrum of the probe will reveal a discrete Compton line. When the scatterer is not in a momentum eigenstate initially, the energy spectrum of the probing particles is no longer a discrete line, but will be broadened due to the momentum uncertainty of the scatterer. It can be shown that under conditions of the impulse approximation (Eisenberger and Platzman 1970), i.e. high scattering angles, the resulting Compton profile (CP) in the spectrum is a direct image of the momentum distribution of the target electrons in the ground state. Compton scattering (CS) can thus be used to obtain valuable information on the electronic properties of solids directly, in a momentum representation. Especially in metals and semiconductors, which have rather delocalized charge carriers, and consequently fairly small momentum uncertainties, Compton scattering is a powerful method; it has also been used successfully in covalent systems (Williams 1977, Williams and Thomas 1983, Cooper 1971).

Photon Compton scattering has almost evolved to a routine application with γ-rays or synchrotron radiation. Due to the inevitable background signal, direct detection of CPs is rare (Reed and Eisenberger 1972). Rather, it is customary to subtract two CPs, obtained with different orientations of the crystal. This procedure is supposed to remove the background completely, the differential CPs so obtained show the momentum anisotropy of the target electrons.

0953-8984/93/397173+16$07.50

A transmission electron microscope (TEM) equipped with an electron energy-loss spectrometer is well suited to Compton experiments on a microscopic scale by a technique known as electron Compton scattering from solids (ECOSS), first introduced by Williams and co-workers (1984) about ten years ago. This technique has a number of advantages compared to the standard photon scattering techniques:

(a) at typical scattering angles the scattering cross section for electrons is larger by five orders of magnitude than for photons;

(b) the brightness of modern electron sources surpasses that of photon sources by two orders of magnitude;

(c) post-specimen electron optical devices allow a much better momentum resolution than photon Compton scattering devices;

(d) focusing of electrons onto the specimen allows spatial resolutions of some nm, in principle, compared to mm in photon work.

From (a) and (b) it is evident that the sensitivity of ECOSS enormously exceeds that of photon Compton scattering; the duration of an experiment can be reduced from several hours for photon scattering to minutes.

The major drawback in ECOSS relates to (a) above. The large cross section for scattering of electrons in matter brings about a huge background which easily overrides the Compton signal.

A related problem is the strong Bragg scattering for electrons. Due to the short extinction length, dynamical diffraction theory must be used for electrons whereas the extinction lengths on a scale of mm to cm for photons allow us to consider Bragg scattering as a faint perturbation. This may be the reason that no real progress has been reported on ECOSS since the early attempts a decade ago.

The scope of this paper is to report the present state of ECOSS experiments and to demonstrate, by experimental example, how Compton measurements in the TEM can be performed properly. We show that the inherent difficulties of ECOSS can be overcome by a careful selection of the experimental set-up and by use of sophisticated data processing (suitable background modelling and deconvolution routines).

The central quantity in CS, the CP

$$J(p_z) = \int \mathrm{d}^2 p_{xy}\, \rho(p_{xy}, p_z) \tag{1}$$

is the projection integral of the momentum density ρ onto the direction of the scattering vector q. Here and in the remainder of this paper, the coordinate system is chosen such that q defines the z direction. Under conditions of CS, that is, for single scattering and in the impulse approximation (Eisenberger and Platzman 1970), the double differential scattering probability for inelastic electron scattering relates to the CP as

$$\mathrm{d}^2\sigma/\mathrm{d}E\,\mathrm{d}\Omega = [2me^2/(\hbar q)^2]^2(k_b/k_a)(m/4\pi^2 q)J(p_z) \tag{2}$$

where q is the modulus of the scattering vector. The energy loss E on the left is given by p_z as

$$E = E_{max} + p_z(2E_{max}/m_e)^{1/2} \tag{3}$$

where E_{max} is

$$E_{max} = E_0(1 + E_0/2m_e c^2)\sin^2\theta. \tag{4}$$

The energy E_0 is the primary relativistic kinetic energy of the probe electron; θ is the scattering angle, which is related to the momentum transfer q such that $\theta = q/k_a$. Equation (4) is the starting point for all data analysis in CS since it is used to convert the energy scale of a measured loss spectrum to a momentum scale.

In section 2 we discuss the most favourable experimental conditions. We analyse the sources of experimental error and calculate the momentum resolution in the present experiment, giving an estimate of the ultimately achievable resolution. In section 3 we describe the various background contributions. A method to deal with the background, based on simulations of momentum-resolved multiple inelastic scattering, is presented. The broadening of the CP caused by plasmon excitation can be removed by deconvolution.

2. Experiment

2.1. ECOSS in the TEM

In terms of electron microscopy ECOSS is electron energy loss spectrometry (EELS) in diffraction mode at high scattering angles, performing an energy scan across the Bethe ridge. To reduce multiple scattering the primary beam energy E_0 should be as high as possible—200 keV in the present case. The spectrometer aperture is located in the optical axis of the microscope just below the viewing screen; the diffraction pattern is shifted by deflection coils located between the focal plane and the image plane of the objective lens to select a scattering angle greater than zero. Previous simulations (Su *et al* 1992) have shown that the contributions of multiple scattering and elastic background are less if the spectra are taken at high momentum transfer, therefore the scattering angle in our measurements was chosen to be around 63 mrad which leads to count rates of about 10 Compton-scattered electrons s^{-1} impinging on the detector.

In parallel EELS the sensitivity of the detection system is enhanced by a factor of some 100 as compared to serial detection, which is a prerequisite for experiments with such low count rates. The limit concerning the count rate is determined by the detector's dark signal, which is equivalent to 70 electrons s^{-1} if the detector is cooled to $-15\,^{\circ}C$; for a comprehensive discussion of the performance of the GATAN 666 PEELS under the conditions of a low-count-rate experiment see the article by Jonas and Schattschneider (1991).

Parallel detection reduces the dwell time for a single measurement from hours to several minutes, nevertheless this is still a rather long time from the microscopist's point of view. High voltage and lens currents are stable enough during that time, but specimen drift and irradiation-induced changes of the specimen, such as mass loss, radiation damage, amorphization, hydrocarbon contamination and oxidation impose severe restrictions. It turned out that cooling the specimen chamber by a cold trap kept at liquid-nitrogen temperature did not sufficiently reduce the hydrocarbon contamination on the specimen surface. A cooling specimen holder at about $-100\,^{\circ}C$ prevented contamination. Quantitative microanalysis with EELS indicated no detectable amount of carbon on the specimen, even after an exposure time of 30 min, if the specimen is cooled.

Single-crystal silicon was chosen as a test material since it is well documented in literature, easy to prepare for the microscope and quite inert to oxidation. Preceeding experiments with aluminum showed that materials which easily oxidize are not suited for this kind of measurement. The reason is that we have to use specimens as thin as possible to reduce multiple scattering and therefore a thin surface layer containing oxygen changes the shape of the CP markedly.

2.2. Resolution

The resolution δp_z of the momentum component p_z that can be achieved in a Compton experiment in the TEM depends on the momentum transfer resolution δq in the diffraction plane, determined by the angle of convergence of the primary electron beam incident on the specimen, spherical and chromatic aberration of the post-specimen magnetic lenses and the diameter of the spectrometer entrance aperture, and further by the energy resolution δE, which is given by the energy spread of the electron source and the energy-resolving properties of the detection system.

2.2.1. Energy resolution. A hairpin tungsten filament provides an electron beam of about 2 eV full width at half maximum (FWHM) thermal energy spread. For the purpose of detection in a linear photodiode array the electrons are converted to photons by a single-crystal YAG scintillator. One electron produces approximately 1800 photons within the scintillator; the signal from a single electron spreads over some tens of μm in the scintillator; therefore the primary signal is broadened by convolution with the line spread function (LSF), which is defined as the signal of a point source on the photodiode array; for an LSF of 3.5 channels FWHM the energy resolution decreases to $\delta E = 8$ eV FWHM (zero loss) (Jonas and Schattschneider 1991).

The effect of the energy resolution may be found by differentiating (3) and (4):

$$\delta p_z = \delta E (2E_{\max}/m_e)^{-1/2}. \tag{5}$$

δp_z decreases with increasing momentum transfer (i.e. increasing $E_{\max}$). For a typical wave-number transfer of about $q = 16$ Å^{-1}, which corresponds to a Compton maximum at $E_{\max} = 974$ eV, the momentum resolution due to finite energy resolution is calculated as $\delta p_z^E = 0.035$ a.u.†. The shape of the resulting resolution function $f_e(p_z)$ is assumed to be of Gaussian type (see figure 4), the variance calculates to $\sigma_e^2 = (\delta p_z(\text{FWHM})/1.18)^2 = 0.0009$ a.u.^{2}.

2.2.2. Momentum transfer resolution δq. The resolution limiting factors which will be discussed in the following produce a circular disc of almost constant intensity in the diffraction plane (q_x, q_y):

$$F(q_x, q_y) = \begin{cases} \text{constant} & r_q \leqslant \Delta q/2 \\ 0 & r_q > \Delta q/2 \end{cases} \qquad r_q = \sqrt{q_x^2 + q_y^2} \tag{6}$$

where Δq is the diameter of the disc in units of wave number.

(a) Pre-spectrometer lens aberrations. As stated above the PEELS is mounted below the TEM column so that the electrons have to pass through the microscope imaging lenses before they reach the spectrometer. As a result of aberrations (Kruit and Shuman 1985, Titmarsh and Malis 1989, Yang and Egerton 1992), a single point in the diffraction plane is broadened into a disc of confusion on the viewing screen. The spectrometer aperture which selects the scattering angle is located almost in the same plane, therefore effects of lens aberrations have to be taken into account.

In diffraction mode, spherical aberration is proportional to the third power of the radius of the selected area aperture (SAA), thus its influence is rapidly reduced by narrowing the SAA.

† The unit of momentum p_z will be given in 'atomic units' as usual in Compton scattering literature; 1 a.u. $= \hbar a_0^{-1}$, $\hbar \equiv 1$. To convert the momentum given in units of wave number to atomic units: 1 a.u. $\equiv 0.529$ Å^{-1}.

Chromatic aberration results in an overfocusing of the diffraction pattern generated by electrons that have suffered a certain amount of energy loss E proportional to the ratio E/E_0. Due to the fact that the intensity of the zero-loss electrons exceeds that of the high-loss electrons, the contribution of the high-loss electrons is invisible on the screen; the diffraction pattern visible on the viewing screen is made up by zero-loss electrons. For electrons which have suffered an energy loss E the central diffraction spot becomes a disc of diameter D_c at the plane of the spectrometer entrance aperture (Yang and Egerton 1992), the momentum uncertainty due to chromatic aberration being

$$\Delta q_c = (D_c/L)k_0 = A(E/E_0)dk_0. \tag{7}$$

Here, L is the camera length, E_0 is the primary beam energy, k_0 is the primary beam wave number ($k_0 = 250.5$ Å^{-1} for 200 keV), d is the diameter (in units of μm) of the specimen contributing to the diffraction pattern, determined either by the spot diameter of the incident beam or by an SAA. A is a constant which depends on the chromatic aberration coefficients of all post-specimen lenses and their respective magnifications.

By means of a high-voltage wobbler which periodically alters the acceleration voltage of the microscope between V_0 and $V_0 - \Delta V$, the effect of chromatic aberration can be made visible; ΔV was measured with PEELS to be 1900 V. We measured D_c for all SAA diameters availiable, with the help of a printed mm scale on our viewing screen. The measurements were carried out under the condition of parallel illumination, determined from the diffraction pattern. The quantity A can be calculated as the gradient of the least-squares-fitted line in figure 1 to be $A = 4.77 \times 10^{-2}$ μm^{-1}.

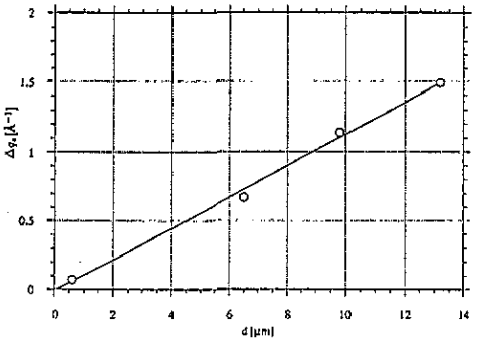

Figure 1. Measured diameter Δq_c of the disc of confusion caused by chromatic aberration due to electrons of $E = 1900$ eV energy loss as a function of the diameter d of the illuminated specimen area (parallel illumination, d is determined by an SAA).

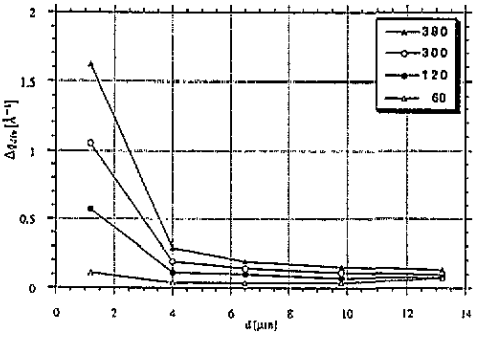

Figure 2. Measured diameter Δq_{div} of the disc of confusion caused by divergency of the primary beam as a function of d (divergent illumination, d is determined by the spot diameter). The parameter is the diameter of the condenser aperture d_{cond} given in units of μm.

(b) Beam angular divergence. As will be shown later the count rate is the crucial parameter in ECOSS. So, the task is to obtain as much primary intensity as possible on the area of the specimen contributing to the diffraction pattern, which we have seen above has to be reduced in order to minimize chromatic aberration. Focusing the beam, on the other hand, results in an enhancement of the momentum uncertainty due to an increased angular divergence of the electron beam impinging on the specimen, which can be decreased by selecting a narrow condenser aperture, leading to a reduction of the primary intensity.

The angular divergence as a function of the irradiated area diameter d was measured from the size of the spots in the diffraction pattern, for several condenser aperture diameters d_{cond} (380, 300, 120 and 60 μm). Figure 2 shows the momentum uncertainty Δq_{div} due to the angular divergence as a function of spot diameter d on the specimen; it should be kept in mind that narrowing the diameter d_{cond} from 380 μm to 60 μm reduces the primary intensity by a factor of 40.

The combined convolution function $F_{\mathrm{c,div}} = F_{\mathrm{c}} * F_{\mathrm{div}}$ (* denotes convolution) due to chromatic aberration and angular divergence as a function of d for an energy loss $E = 1000$ eV is displayed in figure 3; calculated for the set-up with $d_{\mathrm{ap}} = 120$ μm condenser aperture, which was found to be a reasonable compromise between the requirements of momentum resolution and the count rate. Since for large d, $\Delta q_{\mathrm{c,div}}$ is dominated by chromatic aberration (figure 1), leading to a linear decrease as a function of d, whereas for small d, $\Delta q_{\mathrm{c,div}}$ is equal to Δq_{div} (figure 2); a minimum in $\Delta q_{\mathrm{c,div}}$ is expected to exist for values of d around 3–4 μm; this is found to be true from figure 3.

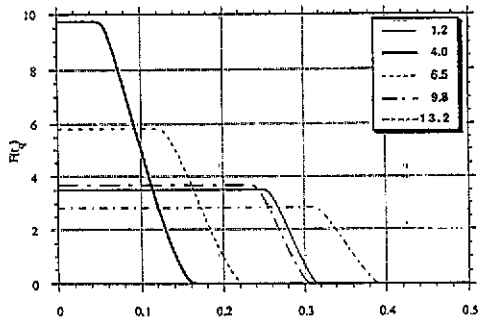

Figure 3. Combined convolution function $F_{\mathrm{c,div}} = F_{\mathrm{c}} * F_{\mathrm{div}}$ due to chromatic aberration and angular divergence for an energy loss $E = 1000$ eV. The parameter is the diameter d of the illuminated area.

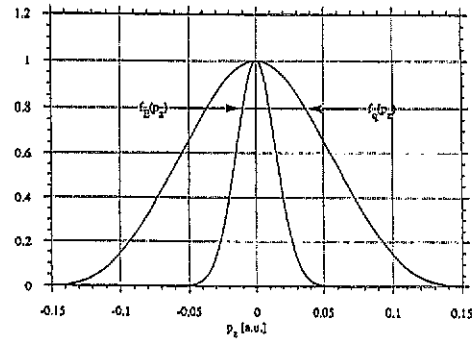

Figure 4. Momentum resolution functions $f_q(p_z)$ due to a limited momentum transfer resolution, and $f_E(p_z)$ due to a limited energy resolution.

(c) Spectrometer entrance aperture SPA. Finally, the SPA, selecting a small area of the diffraction plane, contributes to the momentum uncertainty as

$$\Delta q_{\mathrm{ap}} = (d_{\mathrm{ap}}/L)k_0 \tag{8}$$

where d_{ap} is the diameter of the SPA. It can, in principle, be chosen to be very small by increasing the camera length while decreasing the diameter of the aperture, but it turns out that we are limited in reducing Δq_{ap} very soon by the requirements concerning the count rate; furthermore, it is not useful to choose Δq_{ap} to be distinctly below $\Delta q_{\mathrm{c,div}}$, since this would be a waste of intensity without gain in resolution. Therefore the spectra were taken at a camera length of 1820 mm and an SPA of 2 mm resulting in $\Delta q_{\mathrm{ap}} = 0.28$ Å^{-1}.

The three rectangular functions from above are to be convoluted with each other to give the final momentum transfer resolution function $F(q_x, q_y)$, which decreases the resolution within the diffraction pattern. The resulting scattering profile from a non-δ-like scattering source is a convolution

$$CP_{\mathrm{tot}}(q_0) = \int_{q_0-\Delta q/2}^{q_0+\Delta q/2} f_q(q' - q_0) CP(q')\,\mathrm{d}q' \tag{9}$$

where q_0 is the mean momentum transfer. We may call the weight function

$$f_q(q') = \int F(q', q_y)\,\mathrm{d}q_y \tag{10}$$

an effective resolution function, enabling us to quantify the momentum resolution δp_z^q due to limited momentum transfer resolution δq in our experiment.

Figure 4 shows the resolution functions $f_q(p_z)$ and $f_e(p_z)$ due to a limited momentum transfer resolution and a limited energy resolution, respectively. It is obvious that $f_q(p_z)$ with $\delta p_z^q = 0.13$ a.u. is dominant compared to $\delta p_z^E = 0.035$ a.u. caused by δE. The respective variances add to give

$$\sigma_{\mathrm{tot}}^2 = 0.013 \text{ a.u.}^2 \rightarrow \delta p_z^{\mathrm{tot}} = 0.135 \text{ a.u. (FWHM)}.$$

This momentum resolution $\delta p_z^{\mathrm{tot}}$ is of the order of the best photon experiments at present (Schmitz *et al* 1990), but it is rather poor compared to the possibilities of ECOSS. All three major contributions to δp_z could be lowered independently of each other, as is quite obvious from figures 1 and 2. The thing to do would be to narrow the SAA while opening the spot size, making the beam incident on the specimen almost parallel, and to increase the camera length while narrowing the spectrometer aperture diameter d_{ap}. So, if we could provide a detector system capable of detecting count rates near the single-electron region, extremely high momentum resolutions could be reached.

By cooling the PDA with liquid nitrogen, reducing the dark current, and the use of direct detection, enhancing the signal in the PDA per primary electron, a 60-fold increase in sensitivity of the electron detection system is supposed to be possible (Quandt *et al* 1990). The minimum value of Δq_{ap} that can be selected in our microscope is given by $\mathrm{SPA}_{\mathrm{min}} = 1$ mm and the maximum camera length $L_{\mathrm{max}} = 3200$ mm, resulting in $\Delta q_{\mathrm{ap}}^{\mathrm{min}} = 0.08$ Å^{-1}; this would reduce the count rate by a factor of 12 compared with the conditions discussed above. The remaining gain in sensitivity can be used to decrease the values of Δq_{c} and Δq_{div}, so that a momentum resolution of $\delta q = 0.1$ Å^{-1} ($\equiv 0.05$ a.u.) with the Jeol 200CX appears feasible.

2.3. Scattering geometry

Using single-crystal specimens to measure directional CPs, care has to be taken in choosing a proper scattering geometry. The reason is that strong contributions from Bragg–Compton channel coupling may overlap the directly scattered Compton intensity and alter the result dramatically. Each Bragg beam, having been diffracted through a large angle relative to the incident beam, may undergo Compton scattering into the direction of the spectrometer aperture. A set of various CPs with different maxima, widths and directions in momentum SPAce is superimposed on the single scattering profile. Coherent effects (superposition of amplitudes instead of intensities from different directions) may also influence the result (Schülke and Mourikis 1986).

Williams (1987) calculated the multiple scattering contributions due to Bragg scattering in the high-energy and high-momentum-transfer regime using a multi-slice approach that allows for dynamical scattering, and treating each Bragg beam as a source of CS. The calculation showed that it is impossible to obtain a useful result for a single crystal in a zone-axis orientation, so the goal is to reduce the number of Bragg-diffracted beams which may contribute to the measurement and to find a scattering geometry where CPs of one scattering angle and equivalent directions in momentum space can be measured.

This can be achieved by tilting the specimen away from the zone axis into a two-beam case; placing the spectrometer aperture exactly on the axis of symmetry we measure two CPs of the same scattering angle (see figure 5)†. The total intensity J_t scattered into the aperture can be written as follows:

$$J_t \propto I_0 J(p_z \parallel hkl) + I_G J(p_z \parallel h\bar{k}l) + J_{\text{coherent}}. \tag{11}$$

I_0 and I_G are the intensities of the unscattered and the Bragg-diffracted beams, respectively, due to dynamical diffraction. Coherent scattering has, in principle, to be taken into account because the initial electron state is no longer a plane wave with wave vector $\boldsymbol{K}_a$, but a coherent superposition of two plane waves $\boldsymbol{K}_a$ and $\boldsymbol{K}_a + \boldsymbol{G}$. It can be shown that the coherent-scattering part in equation (11) vanishes for a two-beam case in the exact Bragg position (i.e. when the deviation parameter $w = 0$) (Jonas 1993).

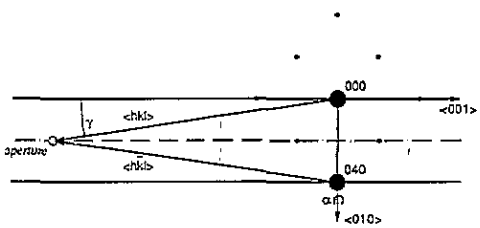

Figure 5. Two-beam scattering geometry.

Since the CP as a function of the direction of the scattering vector has the same symmetry as the crystal lattice, the CP parallel to the $\langle hkl \rangle$ direction is equal to that parallel to the $\langle h\bar{k}l \rangle$ direction in momentum space for the case of silicon, which has a diamond type lattice.

Using the two-beam technique has its consequences upon the directions p_z availiable for the measurement. We will explain this in more detail for a (040) two-beam case adjacent to the $\langle 1, 0, 0 \rangle$ zone axis (figure 5). Tilting the crystal about the $\langle 0, 1, 0 \rangle$ direction out of the $\langle 1, 0, 0 \rangle$ zone axis diminishes the intensity of the Bragg spots parallel to the (0, 4, 0) systematic row to almost zero. The rotation angle α necessary to achieve a proper two-beam condition ranges about 5–7° depending on the selected Bragg reflection. (The direction of the axis of symmetry changes from $\langle 0, 0, 1 \rangle$ to $\langle 1, 0, 10 \rangle$ when tilting by α).

The momentum component p_z actually measured lies within the $\langle 10, 0, 1 \rangle$ plane, $\gamma°$ away from the direction of the symmetry axis; γ is given by $\sin\gamma = k_G/2q$. For a typical scattering angle $q = 16$ Å^{-1} and $k_{0,4,0} = 4.6$ Å^{-1}, we obtain $\gamma = 8.2°$ and finally $p_z \parallel \langle 2, 3, 20 \rangle$.

The scattering vector does not coincide with a high-symmetry direction any longer. For an accurate comparison of experimental CPs with theoretical predictions, the deviation from a high-symmetry direction must be taken into account. For the present purpose, it suffices to realize that the direction $\langle 2, 3, 20 \rangle$ is close enough to $\langle 0, 0, 1 \rangle$ for an evaluation of the principal validity of the experiment and the data processing. (The angle between $\langle 2, 3, 20 \rangle$ and $\langle 0, 0, 1 \rangle$ is approximately 10°.)

† When using a low-indexed reciprocal lattice vector for the two-beam case, such as (2, 2, 0), the higher-order contributions from the systematic row are still strong, which results in a superposition of CPs from additional directions. With the (4, 0, 0) case for Si, the excitation errors for the other reflections of the systematic row are high enough that the respective intensities can be neglected.

2.4. Spectrum processing

Setting up the microscope as described above leads to an average count rate of about 10 scattered electrons s^{-1} at the Compton maximum, at a momentum transfer of $q = 16$ Å^{-1}. Although the photodiode array is cooled by a Peltier cooler to about -15 °C, the amount of dark signal produced by the PDA is equivalent to 70 scattered electrons s^{-1}. It is obvious from figure 6 that the count rate is at the limit of detectability and we cannot afford to reduce the primary intensity for the purpose of increasing the momentum resolution.

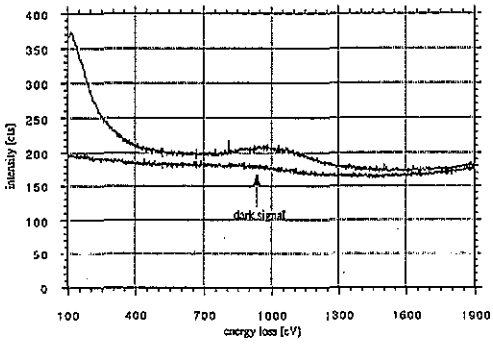

Figure 6. Total signal and dark signal for a 50 s dwell time measurement.

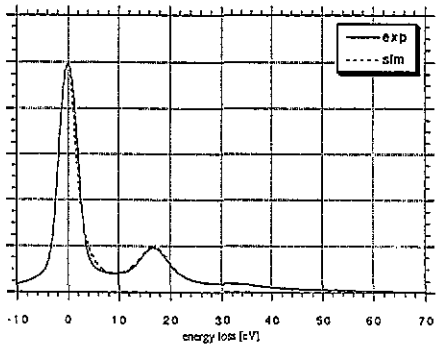

Figure 7. Experimental and simulated low-loss bright-field spectrum for a specimen of thickness $D_p = 0.35$.

18 spectra, with a dwell time of 50 s each, have to be acquired to give one spectrum with reasonable statistics; they are taken under the same experimental conditions except that they are shifted over the photodiode array with respect to each other by a few channels. Each spectrum is first corrected for dark current and intrinsic channel-to-channel gain variations between the 1024 detector elements:

$$\mathrm{spk}^{I}(i) = \frac{\mathrm{spk}(i) - \mathrm{dark}(i)}{\mathrm{gain}(i)} \qquad \sum_{i} \mathrm{gain}(i) = 1 \tag{12}$$

where spk(i) is the total signal in channel i, dark(i) is the respective dark signal and gain(i) is a 'flat-field' spectrum which is measured by defocusing the post-spectrometer quadrupole lenses such that the entire array is uniformly illuminated (Krivanek *et al* 1987, Shuman and Kruit 1985).

Since, for various reasons, the flat-field spectrum cannot be measured exactly in the GATAN 666 spectrometer, we continue the correction process with a more sophisticated method called 'iterative gain averaging' to reduce the noise introduced by channel-to-channel gain variations (Boothroyd *et al* 1990, Schattschneider and Jonas 1993). The method is based on the fact that the signal for a fixed energy loss is measured at different positions on the array and an average is made over the variations in the gain. Gain averaging is capable of reducing all kinds of noise intrinsic to parallel detection, not only channel-to-channel gain variations but also variations in the dark current rate and what is called 'read-out noise'.

The remaining noise due to counting statistics is smoothed by a standard Fourier transform low-pass filter (Press *et al* 1986).

3. The simulation

The output of the processing routine described above can now be compared with theoretical predictions. The problem is that the processed data contain strong—sometimes even dominant—contributions from plural scattering such as combinations of elastic large-angle scattering with low-angle ionization processes.

In order to obtain a better insight into the mechanisms of multiple scattering and how coupling with other scattering events changes the shape of the pure CP, we simulate energy-loss spectra at large momentum transfer for a homogeneous isotropic medium under the assumption that multiple scattering obeys Poissonian statistics and that channel coupling is isotropic (Su *et al* 1992). The total spectra include plasmon scattering, isotropic elastic scattering, L-shell ionization and CS; Bragg scattering can be taken into account by regarding each diffracted beam as a new source of scattering.

In Fourier space the total energy and angular distribution of scattered electrons in an isotropic medium can be written as

$$\tilde{P}_{\mathrm{tot}}(\omega, \rho) = \exp(-D)\exp[D\tilde{f}(\omega, \rho)]. \tag{13}$$

The tilde denotes a Fourier transform with respect to the energy variable $E \rightarrow \omega$ combined with a Hankel transform with respect to the scattering angle $\theta \rightarrow \rho$. The parameter D is the specimen thickness t given in units of the total mean free path length:

$$D = \frac{t}{\lambda_{\mathrm{tot}}} = \sum_i \frac{t}{\lambda_i} \tag{14}$$

where λ_i are the mean free path lengths of the various scattering events. $\tilde{f}(\omega, \rho)$ is the Fourier–Hankel transform of the energy and angular distribution of the total single scattering function. $\tilde{P}_{\mathrm{tot}}(\omega, \rho)$ can be written in more detail:

$$\tilde{P}_{\mathrm{tot}}(\omega, \rho) = \tilde{P}_0 + \tilde{P}_{\mathrm{e}} + \tilde{P}_{\mathrm{i}} + \tilde{P}_{\mathrm{i,e}} \qquad \tilde{P}_{\mathrm{i}}(\omega, \rho) = \tilde{P}_{\mathrm{pl}} + \tilde{P}_{\mathrm{c}} + \tilde{P}_{\mathrm{pl,c}} \tag{15}$$

where P_0 is the intensity of the unscattered beam, P_{i} gives the intensity for the inelastic events, P_{e} that for the isotropic, high-angle elastic or quasi-elastic scattering which can be approximated by the Lenz formula (Reimer 1989)

$$P_{\mathrm{e}} = \mathrm{d}\sigma_{\mathrm{el}}/\mathrm{d}\Omega \propto 1/(\theta^2 + \theta_0^2)^2. \tag{16}$$

The characteristic angle θ_0 is a free parameter in the simulation.

$\tilde{P}_{\mathrm{pl}}$ is the probability for the characteristic low-energy loss (i.e. the plasmon); it is, assuming that dispersion can be neglected, described in real space by

$$\mathrm{d}^2\sigma/\mathrm{d}\Omega\,\mathrm{d}E \propto \{EE_{\mathrm{pl}}/[(E^2 - E_{\mathrm{pl}}^2)^2 + E^2\gamma^2]\}1/(\theta^2 + \theta_E^2)\Theta(\theta_{\mathrm{c}} - \theta) \tag{17}$$

where E_{pl} is the plasmon energy, which was measured to be $E_{\mathrm{pl}} = 16.9$ eV; the damping parameter γ was chosen such that the FWHM of the plasmon loss is $\Delta E_{1/2} = 4$ eV. The characteristic angle for plasmon scattering θ_E is 4.25×10^{-5} rad for 200 keV electrons; a cut-off angle θ_{c} takes into account that above a certain momentum transfer q_{c} collective excitations are damped to zero; for Si, $q_{\mathrm{c}} = 1.1$ Å^{-1} ($\theta_{\mathrm{c}} = 4.39 \times 10^{-3}$ rad) (Raether 1980).

P_{c} gives the scattering distribution for the high-energy loss events, i.e. L-shell and CS; the K edge is not present at energy losses below 1840 eV and may be ignored for the

present purpose. The double-differential ionization cross section for L electrons, which for large scattering angles is identical to the CP of the ion core, was calculated by means of the SIGMAL2 program (Egerton 1986). A Hartree–Fock calculation (Angonoa *et al* 1981) is used for the valence-electron contribution to the CP.

Hereafter we will refer to the combined elastic–inelastic scattering events as the 'elastic background':

$$\tilde{P}_{i,e}(\omega, \rho) = \tilde{P}_{tot} - \tilde{P}_0 - \tilde{P}_e - \tilde{P}_l. \tag{18}$$

The cross sections of the different scattering events are matched to each other such that

$$\sigma_{pl}/\sigma_c = x \qquad \sigma_{el}/(\sigma_{pl} + \sigma_c) = C_{el}. \tag{19}$$

As a rough estimate, the ratio x can be determined experimentally by taking a spectrum in bright-field mode including energy losses up to the K edge, $x = 5.5$ follows as the ratio between the area under the plasmon loss and the area under the high-energy loss above the L edge; C_{el} is a free parameter which has to be fitted to the measurement. Noting that $\lambda_i/\lambda_j = \sigma_j/\sigma_i$, the parameter D can be expressed as a multiple of D_p, the specimen thickness in units of the mean free path for plasmon scattering, by equation (19) as

$$D = D_p \cdot [(1 + 1/x)(1 + C_{el})]. \tag{20}$$

For the simulation it is not necessary to know the absolute value of the specimen thickness t; t in units of D_p is found very accurately by comparing a measured bright-field low-loss spectrum with the respective simulated one:

$$\tilde{P}(\omega) = g(\omega) \exp(-D_p) \exp[D_p \tilde{f}_p(\omega)] \tag{21}$$

where $f_p(E)$ is given by the energy-dependent part of equation (17), $g(E)$ is the zero loss which is described by a Lorentzian.

4. Results

In the following section we will discuss the procedure to obtain a pure CP from a set of raw data, measured as described in section 2. The resulting example profile $J(p_z)$, taken in a scattering geometry given above (with $p_z \parallel \langle 2, 3, 20 \rangle$), will be compared with a directional Hartree–Fock calculation (Angonoa *et al* 1981) in the $\langle 0, 0, 1 \rangle$ direction, which is close enough to $\langle 2, 3, 20 \rangle$ for the purpose of this discussion.

4.1. Elastic background

Figure 7 shows the measured and the simulated plasmon spectra for a specimen thickness $D_p = 0.35$. The respective Compton spectrum (momentum transfer $q = 15.4$ Å^{-1}) at the same specimen position together with the simulated elastic background is displayed in figure 8. It has been shown by Su *et al* (1992) that the Compton signal to elastic background ratio increases with decreasing specimen thickness D_p and increasing scattering angle. The two free parameters C_{el} and θ_0 in equations (16) and (19) must be matched to a measured Compton spectrum for each scattering geometry (crystal orientation, scattering angle) anew. This is because expression (16) cannot be a full and rigorous approach

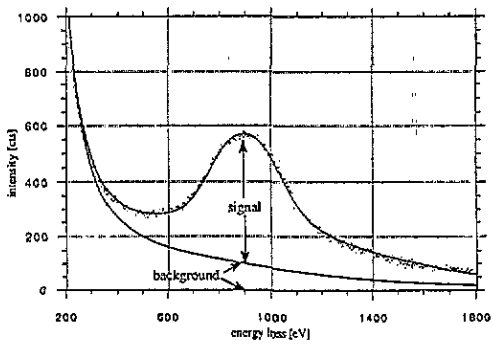

Figure 8. Measured (dots) and simulated total scattering profile at a momentum transfer $q = 15.4$ Å^{-1}, total dwell time $t = 900$ s and specimen thickness $D_p = 0.35$; the simulated elastic background is also shown.

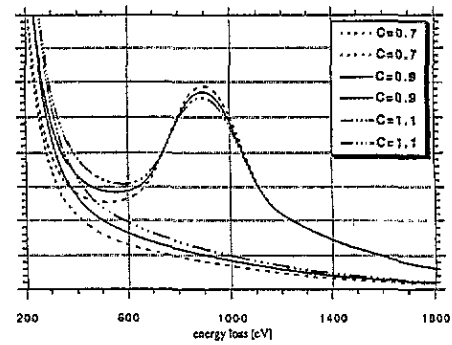

Figure 9. Changes in the total profile with respect to the elastic background contribution when varying the parameter C_{el} in the range $0.7 \leqslant C_{el} \leqslant 1.1$.

to the complicated elastic-scattering processes within a single-crystal specimen, but the surprisingly good agreement with experiment indicates that the model is sufficiently accurate.

Figures 9 and 10 demonstrate how the spectra change when C_{el} and θ_0 are varied. C_{el} has a strong influence on the the signal-to-background ratio—as defined in figure 8—but leaves the shape of the elastic background almost unchanged.

In contrast to C_{el}, the parameter θ_0 does alter the shape of the elastic background, which is easy to explain. If θ_0 is large, the channel coupling is dominated by large-angle elastic scattering followed by one or more low-angle inelastic-scattering events; this leads to a smooth, monotonically decreasing function of energy due to the shape of the L-shell ionization cross section for small scattering angles. As θ_0 decreases, the weight of large-angle inelastic scattering is enhanced, which results in a Compton-like peak in the background function. This is the reason that the standard EELS power-law fitted to the elastic background is a poor model for Compton spectra (Su *et al* 1992), since the function of type AE^{-r} is a suitable approximant to the high-energy loss profile only for small scattering angles.

The best fit to C_{el} is reached when the peak height—as defined in figure 10—of the simulated spectrum is equal to that of the experimental spectrum. Changing the characteristic angle θ_0 leaves the signal-to-background ratio almost unchanged, but it alters the shape in the low-energy region of the spectrum, so θ_0 is best fitted when the shape of the 'pre-edge' structure matches that of the experiment.

After fixing the parameters as described above, the background is subtracted; figure 11 shows the smoothed experimental total spectrum, the calculated elastic background and the CP after background subtraction. The simulated background function overestimates the elastic background in the low-energy-loss region which leads to strong deviations of the profile from the theory in the respective energy region; but in the high-energy-loss region, which is the important one for further analysis, the simulated background appears to be a very accurate estimate of the background. The resulting profile is still influenced by plasmon–Compton multiple scattering and broadened by the effective momentum transfer resolution function $f(q')$, therefore deconvolution has to be performed.

4.2. Deconvolution

Following equation (15) the spectrum P_i consists of single CS P_c and the channel-coupling

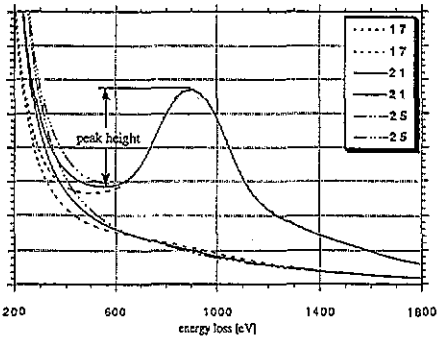

Figure 10. Changes in the total profile with respect to the elastic background contribution when varying the parameter θ_0 in the range $17 \leqslant \theta_0 \leqslant 25$ mrad.

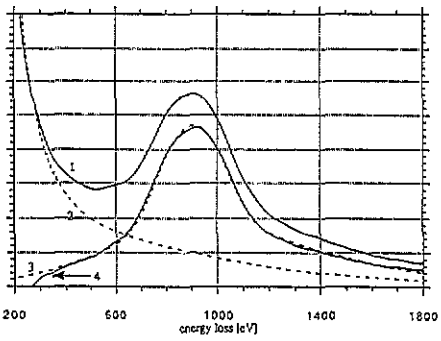

Figure 11. Background subtraction: curve 1, measured total scattering profile (note that the data have been smoothed); curve 2, simulated background contribution; curve 3, simulated profile without background $P_i^{sim}(E; q_0, t)$; curve 4, measured profile after background subtraction $P_i^{exp}(E; q_0, t)$.

part $P_{pl} * P_c$, the pure plasmon-scattering term P_p contributing negligibly in the high-energy-loss region. Several methods to deal with multiple scattering are in principle possible.

First we could think of proceeding in a similar way as in the case of elastic background, i.e. to subtract a calculated channel-coupling contribution $P_{pl} * P_c^{th}$ from a measured P_i^{exp}, starting with a theoretical CP P_c^{th}, to obtain the experimental single Compton part P_c^{exp}. Since $P_{pl} * P_c$ is strong and even exceeds P_c above a specimen thickness of around $D_p = 1.0$, the measured data could be altered in a crucial manner; the final result of the deconvolution procedure (i.e. P_c^{exp}) would become strongly dependent on the theoretical input (i.e. P_c^{th}). To avoid such a direct influence by the theoretical assumptions upon the result, we used an alternative deconvolution procedure which is based on the multiple-scattering simulations.

We suppose that the energy-loss-dependent function $P_i(E; q_0, t)$ for a given specimen thickness t and a fixed momentum transfer q_0 can be written as the convolution of the single scattering profile $P_c(E; q)$ with a folding function $h_p(E; q, t)$ which acounts for plasmon–Compton scattering and the effective momentum transfer resolution function $f(q')$:

$$P_i(E; q_0, t) = \int dq' \, f(q_0 - q') \int dE' \, h_p(E - E'; q', t) P_c(E; q'). \tag{22}$$

The assumption is then that the resulting deconvolution function, which is determined from the simulation as

$$\tilde{g}(\omega; q_0, t) = \tilde{P}_i^{sim}(\omega; q_0, t) / \tilde{P}_c^{th}(\omega; q_0) \tag{23}$$

is a unique function for given momentum transfer q_0 and specimen thickness t, independent of the shape of the CP P_c^{th}. The experimental single CP follows:

$$\tilde{P}_c^{exp}(\omega; q_0) = \tilde{P}_i^{exp}(\omega; q_0, t) / \tilde{g}(\omega; q_0, t). \tag{24}$$

In figure 12 we show the total profile P_i^{exp} which is to be deconvoluted by $g(E; q_0, t)$ and the resulting single scattering profile P_c^{exp}.

4.3. Normalizing the Compton profile

The fact that the CP of the valence electrons in the impulse approximation is symmetric around the Compton peak is used to cut the profile at an 'energy of symmetry' ΔE_{cut}; this energy is determined by means of the simulated profile and is equal to the peak energy of the simulated profile. The high-energy-loss part of the profile is then converted to a momentum scale which refers to the momentum component p_z.

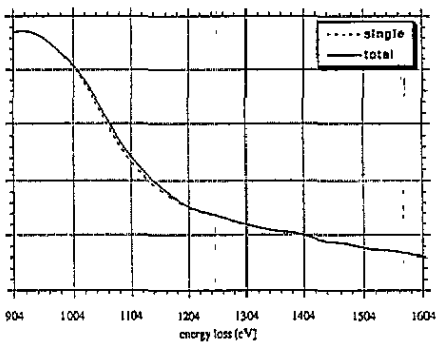

Figure 12. Deconvolution with respect to plasmon–Compton multiple scattering and finite momentum resolution: curve 1, measured total profile $P_{\text{t}}^{\text{exp}}(E; q_0, t)$; curve 2, single profile $P_{\text{c}}^{\text{exp}}(E; q_0)$ as a result of the deconvolution procedure.

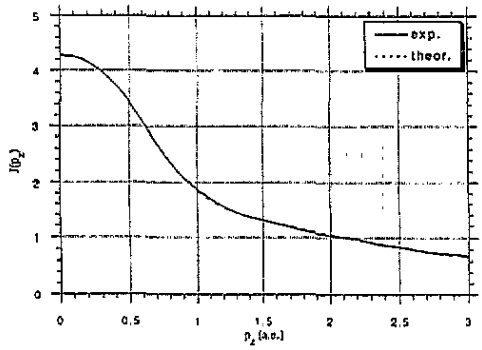

Figure 13. Measured Compton profile $J_{\text{exp}}(p_z \parallel \langle 2, 3, 20\rangle)$ and theoretical CP $J_{\text{th}}(p_z \parallel \langle 0, 0, 1\rangle)$.

In the example of figure 12 the 'energy of symmetry' has been determined to be at $\Delta E_{\text{cut}} = 904$ eV, which is not equal to the energy of the maximum intensity ($\Delta E_{\text{max}} = 916$ eV) of the measured spectrum; we believe that this caused by the uncertainty due to counting statistics. The use of the proper value for ΔE_{cut} is crucial for the conversion to a momentum scale which is obvious from equation (4). After conversion the profiles are to be normalized such that

$$\int_{-\infty}^{+\infty} \mathrm{d}p_z\, J(p_z) = n_{\text{el}} \tag{25}$$

where n_{el} is the number of electrons in the atom ($n_{\text{el}} = 14$ for Si). Since we obtain no useful signal above $p_z = 3$ a.u., the measured spectrum is normalized such that

$$\int_0^3 \mathrm{d}p_z\, (J_{\text{exp}}(p_z) + \text{constant}) = \int_0^3 \mathrm{d}p_z\, J_{\text{th}}(p_z). \tag{26}$$

The constant is added to account for the contribution of the K-shell electrons, which is not included in the measured profile because the K edge is at 1840 eV, far above the energy range of the measured CP. The contribution of the K-shell electrons is almost constant within the momentum range $0 \leqslant p_z \leqslant 3$ a.u.

Figure 13 shows the measured CP in the $\langle 2, 3, 20\rangle$ direction in momentum space compared with the theoretical one (Angonoa *et al* 1981) in $\langle 0, 0, 1\rangle$ direction. The differences between measurement and theory are shown in figure 14; the noise in the profile due to counting statistics is indicated by the error bar, determined from the average input spectrum as $\pm 1\%$ at $p_z = 0$. It can be seen that simulation and experiment agree within the experimental noise limit.

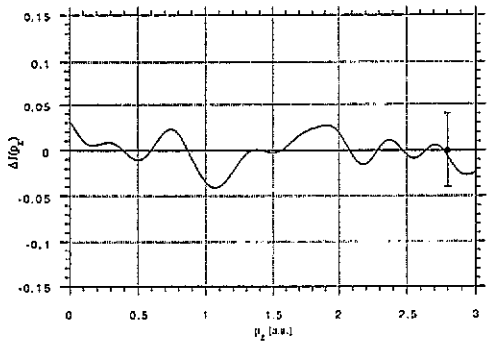

Figure 14. Difference profile $\Delta J = J_{th} - J_{exp}$ between theoretical and measured CPs given in figure 13. The error bar marks the statistical uncertainty at $p_z = 0$.

5. Conclusion

Under favourable experimental conditions, that is, momentum transfers where the impulse approximation is valid; specimens with a thickness of less than 0.5 MFPs of plasmon excitation (that is $\sim$ 80 nm at 200 keV primary energy); prevention of hydrocarbon contamination by proper measures (e.g. a cooling holder); using robust specimens insensitive to radiation damage; and a scattering geometry closely resembling a two-beam case with the scattering vector in a direction of symmetry, it is possible in a TEM to obtain total CPs from areas of some μm diameter with overall sampling times of the order of 1000 s. At present, the momentum resolution is comparable to the case of photon CS, but with single-electron detection in parallel EELS mode the attainable momentum resolution for CS in a TEM should be as low as 0.05 a.u. This makes electron CS a very attractive and still unique method for probing the momentum density of solids on a microscale.

We would like to emphasize that the scope of the above investigation was the development of the method of electron CS in the electron microscope *per se* and not the examination of its applicability in material science. Nevertheless it could be expected that ECOSS will be useful for a range of problems in solid-state physics, especially in highly anisotropic systems such as the two-dimensional electron gas, for example the local momentum density distribution and charge transfer within the Cu–O planes of high-T_c superconductors.

Acknowledgments

We would like to thank Dr D S Su for useful discussions on the simulation procedure. This work was supported by the Austrian Fonds zur Förderung der Wissenschaftlichen Forschung, Projekt P7432-PHY.

References

Angonoa G, Dovesi R, Pisani C and Roetti C 1981 *Phil. Mag.* B 44 413

Boothroyd C B, Sato K and Yamada K 1990 *Proc. 12th Int. Congr. on Electron Microscopy (Seattle, 1990)* (San Francisco: San Francisco Press) p 80

Compton A H 1922 *Phys. Rev.* **19** 267

Cooper M 1971 *Adv. Phys.* **20** 453

Egerton R F 1986 *Electron Energy-Loss Spectroscopy in the Electron Microscope* (New York: Plenum)

Eisenberger P and Platzman P M 1970 *Phys. Rev.* A **6** 415

Jonas P 1993 *Doctoral Thesis* Technische Universität Wien
Jonas P and Schattschneider P 1991 *Ultramicroscopy* **38** 117
Krivanek O L, Ahn C C and Keeney R B 1987 *Ultramicroscopy* **22** 103
Kruit P and Shuman H 1985 *Ultramicroscopy* **17** 263
Press W H, Fannery B P, Teukolsky S A and Vetterling W T 1986 *Numerical Recipes* (Cambridge: Cambridge University Press)
Quandt E, la Barre S, Hartmann A and Niedrig H 1990 *Proc. 12th Int. Congr. on Electron Microscopy (Seattle, 1990)* (San Francisco: San Francisco Press) p 82
Raether H 1980 *Excitation of Plasmons and Interband Transitions by Electrons* (Berlin: Springer)
Reed W A and Eisenberger P 1972 *Phys. Rev.* B **6** 4596
Reimer L 1989 *Ultramicroscopy* **31** 169
Schattschneider P and Jonas P 1993 *Ultramicroscopy* **49** 179
Schmitz J R, Schulte-Schrepping H, Degenhardt J, Mourikis S and Schülke W 1990 *Annual Report of the Hamburger Synchrotronstrahlunslabor HASYLAB* p 613
Schülke W and Mourikis S 1986 *Acta Crystallogr.* A **42** 86
Shuman H and Kruit P 1985 *Rev. Sci. Instrum.* **56** 231
Su D S, Jonas P and Schattschneider P 1992 *Phil. Mag.* B **66** 405
Titmarsh J M and Malis T F, 1989 *Ultramicroscopy* **28** 277
Williams B G (ed) 1977 *Compton Scattering* (New York: McGraw-Hill)
Williams B G and Thomas J M 1983 *Int. Rev. Phys. Chem.* **3** 39
Williams B G, Sparrow T G and Egerton R F 1984 *Proc. R. Soc.* A **393** 409
Williams B G, Uppal M K and Brydson R D 1987 *Proc. R. Soc.* A **409** 161
Yang Y-Y and Egerton R F 1992 *J. Electron Microsc. Technol.* submitted